PERGAMON

International Journal of Heat and Mass Transfer 41 (1998) 3781–3791

International Journal of HEAT and MASS TRANSFER

Detailed heat transfer distributions in two-pass square channels with rib turbulators and bleed holes

Srinath V Ekkad[1], Yizhe Huang[2], Je-Chin Han*

Turbine Heat Transfer Laboratory, Department of Mechanical Engineering, Texas A and M University, College Station, TX 77843-3123, U.S.A.

Received 10 October 1997; in final form 28 February 1998

Abstract

Detailed heat transfer coefficient distributions are presented for a two-pass square channel with a 180° turn. One wall of the channel has periodically placed rib turbulators and bleed holes. Four different configurations of 90° parallel, 60° parallel, 60° V ribs, and 60° inverted V ribs are studied in conjunction with the effect of bleed holes on the same wall. The surface is coated with a thin layer of thermochromic liquid crystals and a transient test is run to obtain the detailed heat transfer distributions. Detailed distributions show distinctive peaks in heat transfer levels around bleed holes and on rib turbulator tips. The 60° parallel, 60° V, and 60° inverted V ribbed channels produce similar levels of heat transfer enhancement in the first pass. However, the 60° inverted V ribbed channel produces higher enhancement in the second pass. Regional-averaged heat transfer results indicate that a surface with bleed holes provides similar heat transfer enhancement as that for a surface without bleed holes although 20–25% of the inlet mass flow exits through the bleed holes.

Nomenclature

b divider wall thickness
d bleed hole diameter
D square channel width or height
e rib height
k thermal conductivity of test surface material
k_a thermal conductivity of air
K_L overall loss coefficient, $\Delta P/(1/2)\rho V_{in}^2$
L length of each pass
$\dot{m}_d$ exit mass flow rate through bleed holes
$\dot{m}_{in}$ inlet mass flow rate
$\dot{m}_{out}$ outlet mass flow rate
Nu local Nusselt number, hD/k_a
Nu_0 Nusselt number from correlation for a straight circular tube, $0.023Re^{0.8}\ Pr^{0.4}$
p rib or bleed hole pitch
P_{amb} ambient pressure
P_{in} inlet pressure
P_{out} outlet pressure
ΔP pressure drop in the channel, $P_{in}-P_{out}$
Pr Prandtl number of air
Re Reynolds number, $\rho V_{in}D/\mu$
t time of liquid crystal color change
T_i initial temperature of test surface
T_w liquid crystal color change temperature
T_m mainstream temperature
V_{in} inlet mean flow velocity
X axial distance from the center of the channel.

Greek symbols

α thermal diffusivity of test surface material
μ dynamic viscosity of air
ρ density of air.

1. Introduction

Modern gas turbine blades have several serpentine channels through which cooling air is passed to remove heat from external surfaces exposed to high temperatures. Coolant passed through several sharp 180° turns and

* Corresponding author.
[1] Mechanical Engineering, Louisiana State University, Baton Rouge, LA.
[2] Motorola, Inc., Austin, TX.

0017–9310/98 $19.00
PII: S0017–9310(98)00099–4

straight sections is ejected on to the external surface through discrete holes on the blade surface. The presence of such bleed holes for external film cooling affects local heat transfer coefficients on the blade internal surface. With the loss of coolant, overall heat transfer augmentation on the internal surface of the channels is expected to be reduced. Several rib configurations have been studied in the past to obtain the most optimum configuration. However, the combined effect of rib turbulators and bleed holes on internal heat transfer augmentation has not been studied to a large extent. The present study focuses on the combined effects of rib turbulators and bleed holes on internal channel heat transfer augmentation.

Several researchers [1-4] have studied the heat transfer and friction characteristics in straight turbulated channels. They studied the effects of Reynolds number and rib geometry (rib height, rib spacing, rib angle and rib configuration) on local, regionally averaged heat transfer distributions, and pressure drop in square ducts with two opposite ribbed walls. Taslim et al. [5] and Taslim and Wadsworth [6] examined the contribution of on-rib heat transfer to the overall heat transfer of a rib-roughened wall with variations in rib angle of attack, rib spacing, or rib height-to-hydraulic diameter. Chandra et al. [7] presented heat transfer and friction results in rectangular channels with one, two, three, and four walls with rib turbulators.

Several studies [8–10] have been presented on local heat/mass transfer distributions in two-pass smooth and ribbed square channels. The above studies used a naphthalene sublimation technique to measure the local mass transfer coefficient on surfaces with rib turbulators. Results from the above studies [8–9] showed that a 60° angled rib produces higher enhancement compared with 45 and 90° ribs. Han and Zhang [10] studied the effect of rib-angle orientation on heat/mass transfer distributions in a three-pass ribbed channel. It was reported that the combined effects of the rib angle, rib orientation, and the sharp 180° turn significantly affect the local mass transfer distributions. The mass transfer technique used in the study provided local heat/mass transfer distributions along three axial lines on the channel surface. Also, the previous studies on two-pass channels provided results for only smooth, transverse (90°), and angled (45 and 60°) rib channels. Ekkad and Han presented detailed heat transfer distributions in the 180° turn region of a two-pass smooth square channel and studied the effect of various rib turbulators on a two-pass square channel without bleed holes [11, 12]. They studied channels with 90° parallel, 60° parallel, 60° V, and 60° broken V-rib configurations. From their results, it is possible to identify the flow separation, reattachment and secondary flow phenomena in the rib turbulated channels from the detailed heat transfer distributions. The present study will compare results with bleed holes to results without bleed holes from ref. [12].

Some studies have focused on the effect of bleed holes on heat transfer in straight channels. Shen et al. [13] studied the heat transfer enhancement within a straight cooling passage with ribs and film cooling holes. Detailed heat transfer contours for one wall enhanced by 90° ribs, and with 90° ribs combined with bleed holes were presented. Taslim et al. [14] studied the effects of bleed holes on heat transfer in trapezoidal straight passages with tapered turbulators. Their focus was on the trailing edge cooling channel which is typically trapezoidal in shape. However, no study with bleed holes along a two-pass channel with or without rib turbulators has been published.

The objective of this study is to present detailed heat transfer coefficient distributions for a two-pass smooth square channel with bleed holes, and a combination of two-pass turbulated channels with bleed holes. Shen et al. [13] and Ekkad and Han [11–12] used a transient liquid crystal method, whereas Taslim et al. [14] used a steady state liquid crystal method for detailed heat transfer measurements. The present study uses the same experimental technique used by Ekkad and Han [11–12]. The detailed heat transfer measurements with bleed holes will help provide better understanding of the heat transfer augmentation mechanism in multi-pass internal turbulated channels with discrete film hole locations. Regionally averaged results from the present study are also compared with results for two-pass turbulated channels without bleed holes [12].

2. Test apparatus

Figure 1 presents a schematic of the experimental set up. The experimental set up consists of an image processing system, flow circuit, and test section. The image processing system consists of an RBG camera connected to a color frame grabber board placed inside the PC. The frame grabber board is programmed through a software package to analyze the color changes during the transient test. The camera is adjusted to view the surface using a color monitor as shown in the figure.

The flow circuit consists of a compressor-based air supply. The air passes through a standard orifice meter which measures the mass flow rate. Air then passes through a 2 kW in-line air heater and a three-way ball diverter valve. The heater input, controlled by a variac, heats up the air to the required temperature. The ball diverter valve routes the air away from the test section when the test is not in progress. A transient test is initiated by switching the valve and letting the hot air into the test section. The flow enters the main section through an entrance duct where the mainstream is allowed to develop before entering the test section.

Figure 2 presents the front view and the top view of the test section. The test section is a two-pass channel

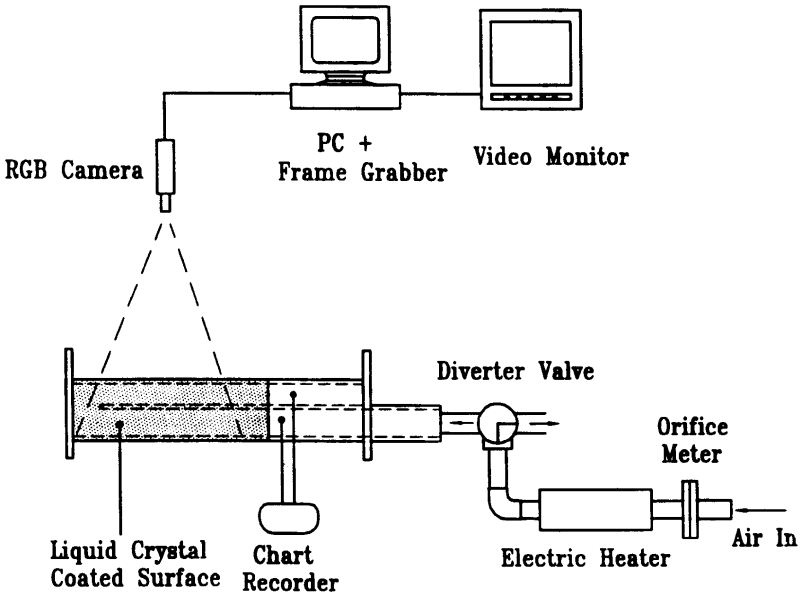

Fig. 1. Experimental setup.

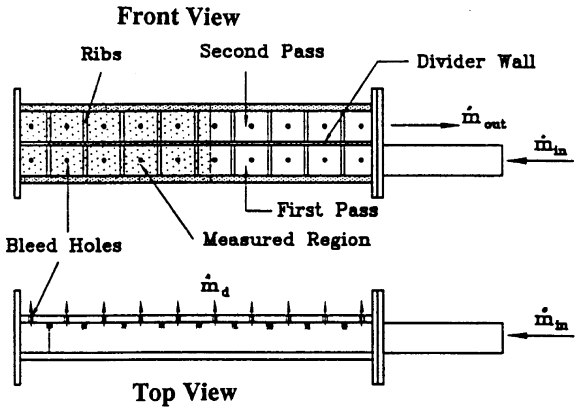

Fig. 2. Two-pass channel with ribs and bleed holes.

with a 5.08 cm square cross-section. Each pass is 60.96 cm long with a L/D ratio of 12. The whole test section is made of plexiglass. The test surface wall (back wall) is made of black plexiglass and sprayed with liquid crystals on the inside. The liquid crystal coated surface is observed through the transparent opposite wall (front wall). The ratio of the two-pass divider wall thickness to the channel width (b/D) is 0.25. The thickness of the plexiglas wall is 1.27 cm. The test surface is shown with bleed holes and 90° parallel rib turbulators. Bleed holes are 0.63 cm in diameter (d) and spaced 10 hole-diameters apart which is the same as the pitch (P) between the ribs.

For the rib-roughened ducts, black plexiglass ribs were attached to the test surface using double-sided tape [12]. Liquid crystals were sprayed following the attachment of the ribs to the surface. Four rib configurations, 90 and 60° parallel, 60° V, and 60° inverted V, are used in this study. Figure 3 presents the rib configurations (with bleed holes) studied. The rib height-to-channel width (e/D) is 0.125 and the rib pitch-to-height ratio (P/e) is 10. A 90° rib was placed along the divider wall in the middle of the 180° turn for all ribbed channels. The ribs are placed such that the bleed holes are nearly in the center of two adjacent ribs.

3. Data reduction

Thermochromic liquid crystals are sprayed uniformly on the test surface using an air gun. The coating is a light spray of thickness in the order of 5–10 μm. Duration of the transient test is much longer than the response of the liquid crystals. The mainstream flow is set to the required flow rate and heated to a required temperature using an in-line air heater. Once the temperature is steady, the diverter valve is quickly changed and the hot air is sent over the test surface causing the liquid crystals to change color. The liquid crystal coated test surface is exposed to the hot air stream during the transient test. The time of color change of the liquid crystals at every point on the test surface is measured using the image processing system and the mainstream temperature is measured using a strip chart recorder.

Local heat transfer coefficient (h) over the test surface coated with liquid crystals can be obtained by assuming

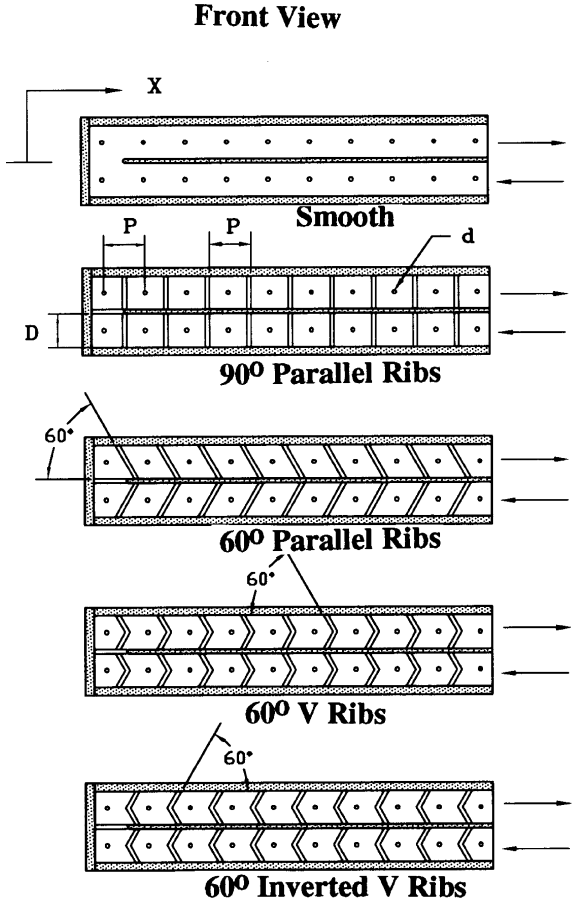

Fig. 3. Test surface geometry with rib configurations.

1-D transient conduction over a semi-infinite solid. Solving the 1-D transient conduction equation with prescribed initial and boundary conditions, one obtains the non-dimensional temperature at the convective boundary surface as

$$\frac{T_w - T_i}{T_m - T_i} = 1 - \exp\left(\frac{h^2 \alpha t}{k^2}\right) erfc\left(\frac{h\sqrt{\alpha t}}{k}\right) \quad (1)$$

Knowing the color change temperature (T_w) from red to green during the transient test, the initial temperature (T_i) of the test surface, the oncoming mainstream temperature (T_m), and the time of color change to green (t) at any location, the local heat transfer coefficient (h) can be calculated from eqn (1). Test conditions are set such that the time of color change on the surface is between 20 and 80 s. This ensures the validity of the semi-infinite solid assumption on the test surface.

The strip chart recorder measures the time-dependent variations of the mainstream temperature at the inlet and outlet of the measured region. The axial variation of temperature in the channel is interpolated from the two measured locations from the chart recorder output. This is to correct the temperature drop which occurs in the channel during the test from inlet to outlet of the measured region. The solution in eqn (1) has to include the gradual changes in mainstream temperature. The time history of the mainstream temperature at every axial location is simulated as a series of time step changes. Using Duhamel's superposition theorem, the solution for the heat transfer coefficient (h) at every location is then represented by

$$T_w - T_i = \sum_{j=1}^{N} \left[1 - \exp\left(\frac{h^2 \alpha (t - \tau_j)}{k^2}\right) \times \operatorname{erfc}\left(\frac{h\sqrt{\alpha(t-\tau_j)}}{k}\right) \right] [\Delta T_{m_{(j,j-1)}}] \quad (2)$$

where $\Delta T_{m(j,j-1)}$ and τ_j are the temperature and time step changes obtained from the chart recorder output. Equation (2) is solved at every point on the surface (250×85 points) to obtain the local heat transfer coefficient.

The experimental uncertainty in the measurement of the convective heat transfer coefficient (h), based on Kline and McClintock's methodology [15], is in the order of $\pm 5.9\%$. The individual uncertainties in the measurement of the time of color change ($\Delta t = \pm 0.5$ s), the mainstream temperature ($\Delta T_m = \pm 1°C$), the color change temperature ($\Delta T_w = \pm 0.2°C$), and the wall material properties ($\Delta\alpha/k^2 = \pm 5\%$). These uncertainties were included in the calculation of the overall uncertainty in the measurement of h.

4. Results and discussion

4.1. Flow measurements

Figure 4 presents the inlet-to-outlet pressure ratio (P_{in}/P_{amb}), over loss coefficient (K_L) and the exit mass flow ratio ($\dot{m}_d/\dot{m}_{in}$) vs Reynolds number for different rib configurations. The pressure drop (ΔP) from the inlet of the two-pass channel to the outlet including the 180° turn is measured. In the present experiment, the pressure at the outlet of the test section (P_{out}) is equal to the ambient pressure (P_{amb}). The inlet pressure at the channel entrance is measured using a pressure tap. The inlet-to-outlet pressure ratio increases with increasing Reynolds number for the smooth and all ribbed channels. The overall loss coefficient for the entire channel is calculated using the formulation, $K_L = \Delta P/(1/2)\rho V_{in}^2$, where V_{in} is the inlet mean flow velocity. The loss coefficients for the ribbed channels are higher than that for the smooth channel as expected. The 90° rib channel has the highest overall loss coefficient compared to the other three channels. However, the difference in loss coefficients between the ribbed channels is small. Overall loss coefficient decreases

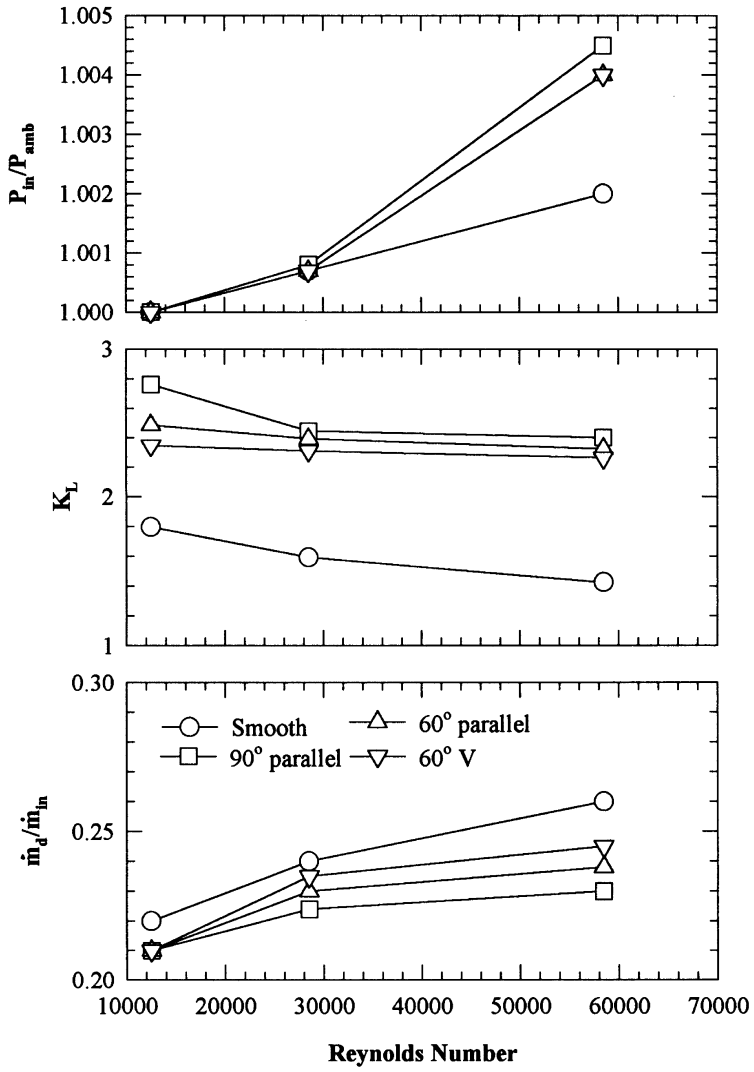

Fig. 4. Inlet-to-outlet pressure ratio, channel flow loss coefficient and exit mass flow ratio vs Reynolds number.

slightly with an increase in Reynolds number for smooth and ribbed channels.

The inlet and outlet mass flow rates of the two-pass channel are measured and the mass flow rate exiting the channel through the bleed holes is determined ($\dot{m}_d = \dot{m}_{in} - \dot{m}_{out}$). The inlet mass flow is measured using the orifice meter and the outlet flow is calculated by measuring the exit flow velocity profile. The exit mass flow ratio ($\dot{m}_d/\dot{m}_{in}$) is thus determined where $\dot{m}_d$ is the mass flow rate exiting through the bleed holes and $\dot{m}_{in}$ is the flow rate entering the channel. Figure 4 shows that the smooth channel has the highest exit mass flow ratio at all Reynolds numbers. Exit mass flow ratio increased with an increase in Reynolds number. Comparing the loss coefficient results and the exit mass flow ratio results, it can be seen that the highest pressure loss coefficient channel with 90° ribs has the lowest exit mass flow ratio. For all four channels, more flow exits out of the first pass bleed holes compared to the second pass holes. This is attributed to the high pressure drop in the flow across the 180° turn.

4.2. Detailed Nusselt number ratio distributions

Figure 5a–e presents the detailed Nusselt number ratio (Nu/Nu_0) distributions at each Reynolds number for all five cases (smooth and ribbed channels with bleed holes). The detailed Nusselt number ratio distributions for channels with ribs only are presented in ref [12]. The local Nusselt number (Nu) is normalized by the fully developed

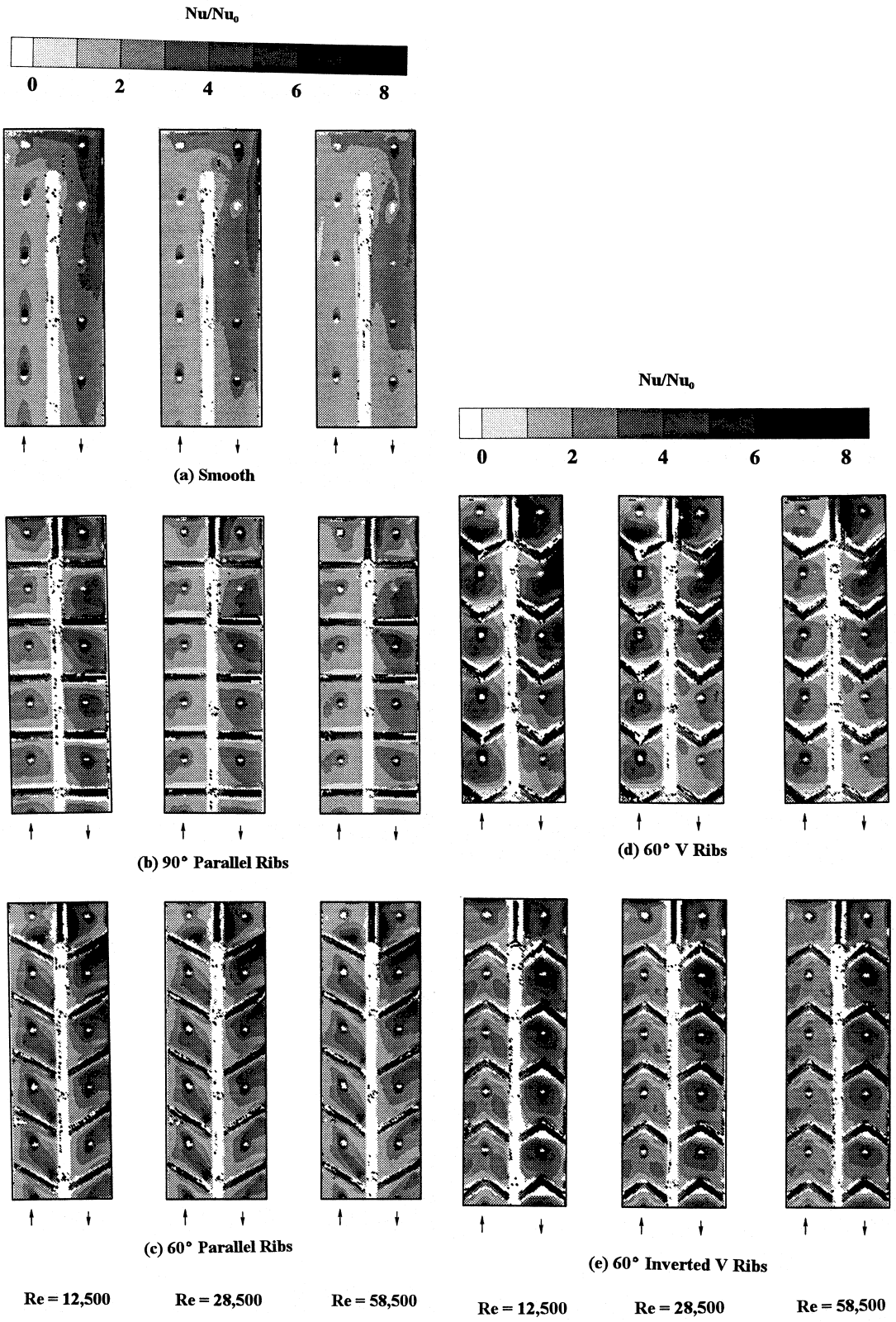

Fig. 5. Detailed Nusselt number distributions for all five channels.

flow Nusselt number ($Nu_0 = 0.023Re^{0.8}Pr^{0.4}$) in a tube for each of the three Reynolds numbers of 12 500, 28 500, and 58 500. The flow Reynolds number is based on the channel hydraulic diameter which is same as the side of the square channel and channel inlet velocity. Nusselt number ratios in the entire channel decrease with an increase in Reynolds number for all smooth and ribbed channels as can be observed clearly in the turn and after-turn regions.

Figure 5a presents detailed results for a smooth surface with bleed holes. In the first pass, there is very little spanwise variation except in the region around and downstream of a bleed hole. Heat transfer is enhanced immediately downstream of a bleed hole. As the flow approaches the 180° turn, there is an increase in Nusselt numbers due to the turning effect. The effect of the turn is visible just downstream of the last hole in the first pass. The flow in the turn region is three-dimensional in nature and is influenced by flow separation at the divider wall tip and the secondary flow induced by the centrifugal forces. The flow tends to move away from the divider wall after the turn due to centrifugal forces and impinges on the opposite wall producing high heat transfer in that region. Further downstream after the turn, Nusselt number values decrease as the effect of the turn reduces. The first two holes in the second pass do not appear to affect the heat transfer distribution. Further downstream into the second pass, there is lesser spanwise variation in the heat transfer distributions with bleed holes enhancing Nusselt numbers just downstream of the holes.

Figure 5b presents the detailed distributions for 90° ribbed channels. The 90° ribs enhance heat transfer compared to a smooth surface. There are greater spanwise and axial variations due to the presence of the ribs. The highest Nusselt number ratios are observed on the top of the ribs. The distributions between adjacent ribs appear periodic in each pass. Heat transfer in the middle region between two adjacent ribs is higher. Heat transfer is very low immediately before and after a rib as the flow separates and reattaches over every rib. Overall, heat transfer coefficients around bleed holes are higher in each pass. In the turn region, the presence of ribs reduces the effect of centrifugal forces on the secondary flow and causes less impingement on the wall away from the divider wall in the turn region and in the second pass. Locally high heat transfer regions are produced by the presence of ribs. Further downstream in the second pass, heat transfer distributions between ribs appear to become more periodic in nature as the effect of the turn reduces.

Figure 5c presents detailed distributions for the 60° ribbed channel. The ribs in the first pass are angled away from the divider wall and the ribs in the second pass are angled toward the divider wall. There is a 90° rib in the turn region. The 60° ribbed channel produces higher Nusselt numbers compared to the 90° ribbed and smooth channels. Similar to the 90° ribbed channel, heat transfer distributions appear periodic between adjacent ribs and the highest Nusselt numbers are obtained on the top of the ribs. The secondary flow moves away from the divider wall towards the outer wall in the first pass. Highest heat transfer regions are present immediately downstream of the ribs near the divider wall and decreasing towards the next rib. The bleed holes appear to have the same effect on heat transfer, particularly in the region immediately downstream of the holes. In the turn region, heat transfer before and after the 90° rib is low. The secondary flow in the second pass moves from the outer wall towards the divider wall. Nusselt numbers are higher near the outer wall and decrease towards the divider wall. Further downstream, the Nusselt numbers decrease as the effect of the turn reduces and flow becomes periodic between the ribs.

Figure 5d presents detailed distributions for the 60° V ribbed channel. The direction of the V shape is the same for both the passes of the channel. A 90° rib is placed in the middle of the turn. The Nusselt numbers are highest on top of the ribs through the test channel. In the first pass, the ribs attack angle, V, is pointed opposite to the flow direction. Two secondary flow structures are formed at the tip of the rib in the middle of the channel. Nusselt number ratios between the ribs are almost uniform except around the bleed hole and closer to the channel walls. Just downstream of every rib, there is a low heat transfer region which is due to the flow separation at the rib tip. The Nusselt number ratio distributions in the first pass appear periodic between ribs. In the after-turn region, Nusselt number ratios are higher near the outer wall and very low near the divider wall. This is due to the centrifugal forces induced by the sharp 180° turn. The flow near the outer wall has a higher velocity compared to the flow near the divider wall. This causes uneven mixing and increases spanwise variations in the Nusselt number ratio distributions. In the second pass, the rib attack angle is inverted with the V-shape pointed along the flow. The inverted V shape is expected to enhance mixing of the two secondary flow structures induced by the turn. However, it appears to have very little effect on the secondary flow. Further downstream of the turn, Nusselt number ratios between ribs are still higher near the outer wall compared to the divider wall. The bleed holes show some effects on Nusselt number ratios.

Figure 5e presents detailed distributions for the 60° inverted V ribbed channel. The direction of ribs are opposite to the 60° V ribbed channel. In the first pass, the V shape is pointed along the flow direction and in the second pass, it is against the flow direction. There is a 90° rib in the middle of the turn. The Nusselt number on top of the ribs is the highest while the Nusselt numbers immediately before and after the ribs are the lowest, as seen for 90 and 60° parallel ribbed channels. In the first pass, each angled side of the ribs generates a secondary flow from the outer and divider walls towards the center

of the channel. The two high heat transfer regions away from the center of the channel downstream of each rib indicates the secondary flow structure. The two secondary flows appear to coalesce upstream of the next rib. There is enhancement of local Nusselt number around the bleed holes. Nusselt numbers in the turn and after-turn regions are very high. Secondary flow structures are generated at the tip of the ribs and move away from the center and this may be the reason there is a high heat transfer region downstream of the rib and decreasing away from the centerline. This behavior is the opposite of that in the first pass. Further downstream, the Nusselt numbers decrease as the effect of the turn reduces. The heat transfer enhancement in the entire two-pass channel might be increased by using V-ribs in the first pass and inverted V-ribs in the second pass.

4.3. Spanwise heat transfer distributions

Figure 6 presents the spanwise-averaged Nusselt number (Nu/Nu_0) distributions for each of the five configurations at $Re = 28\,500$. The trends for $Re = 12\,500$ and $Re = 58\,500$ are similar for all rib configurations (not shown). The bleed hole and the rib locations are indicated as dark circles and dark squares on the figure. The spanwise distributions are presented to indicate the axial heat transfer enhancement variations in the entire channel. The smooth channel Nusselt number ratio values are constant in the first pass as the flow approaches the turn. Nusselt numbers increase in the turn region and decrease further downstream into the second pass as the effect of the turn decreases. Periodic spikes are clearly evident in the first pass immediately downstream of bleed hole locations. The spikes are reduced in the turn, after-turn and second pass. The effect of bleed holes on heat transfer distribution is reduced by the stronger effect of the 180° turn.

The ribbed channels have the additional effect of periodic ribs. The 90° ribbed channel shows a major spike at the rib location and a minor spike just downstream of the bleed hole location. Since, the averaging is spanwise, the other channels with angled and V ribs do not produce as clear a spike as those seen for the 90° ribbed channel. The second pass Nusselt number distribution is affected by the turn and the presence of ribs. Further downstream, the effect of the turn reduces. The angled (60°) and V ribbed channels produce random spikes due to the spanwise averaging. However, the average Nusselt number ratio over the entire channel appears to be higher for these channels compared to that for the smooth and 90° channels.

4.5. Regionally averaged distributions

The local Nusselt number ratios are regionally averaged for every rib pitch of the channel wall in the first pass, in the turn region, and the second pass. Figure 7 presents the effect of rib angle on regionally averaged Nusselt number ratio at each Reynolds number. The distributions are similar for all three Reynolds numbers. In the first pass, 60° parallel, 60° V, and 60 ° inverted V ribs produce almost the same Nusselt number ratios. A smooth channel produces the lowest enhancement. In the turn region, 60° parallel ribs and 60° V ribs produce higher Nusselt number ratios compared to the other ribbed channels. Similar Nusselt number ratios are obtained for 60° parallel, 60° V, and 60° inverted V in

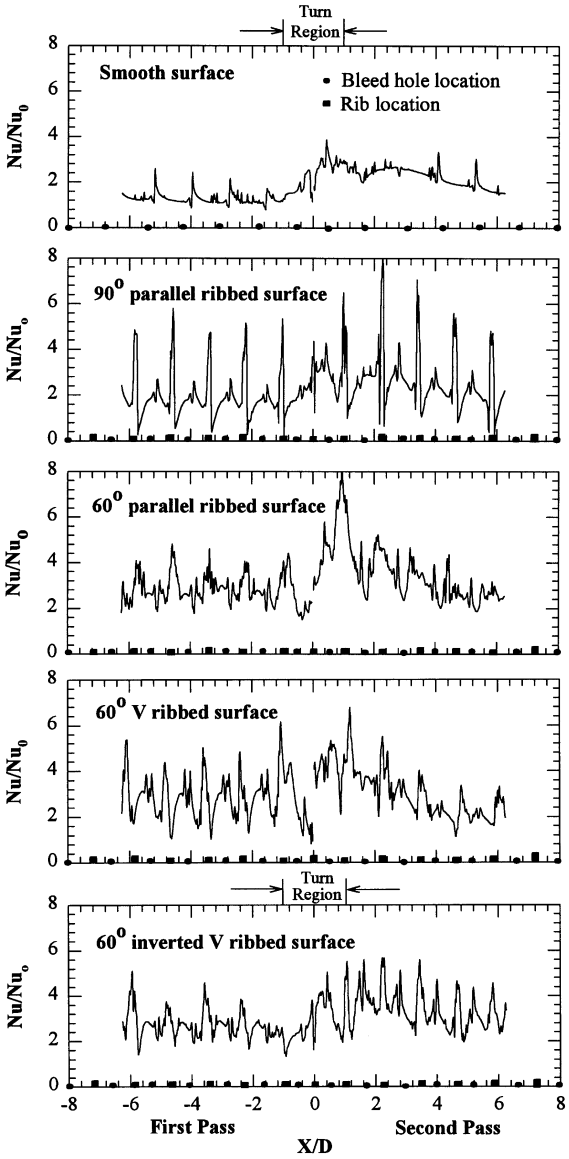

Fig. 6. Spanwise averaged Nusselt number ratio distributions at $Re = 28\,500$.

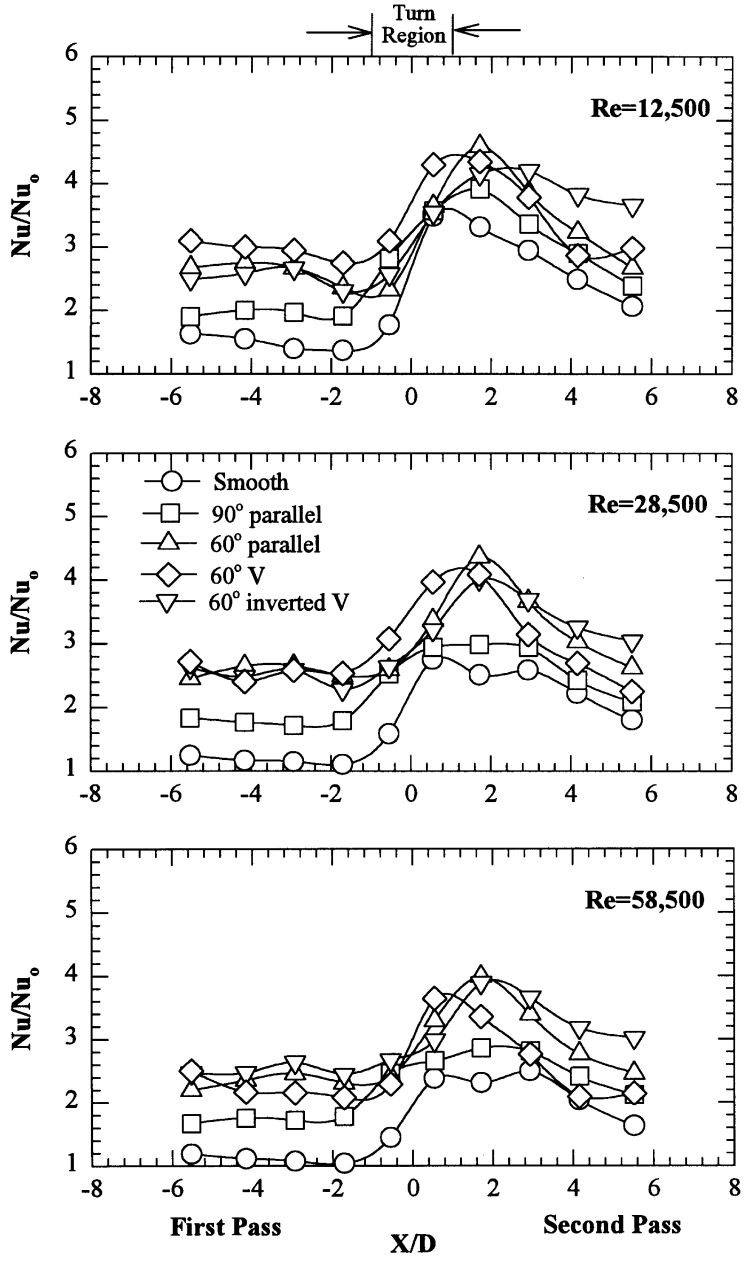

Fig. 7. Effect of rib configurations on regional averaged Nusselt number ratio.

the first pass and turn region. Nusselt number ratios as high as 4.0 are obtained for 60° V ribbed channel in the turn region for $Re = 12\,500$. Further downstream ($X/D > 2.$), 60° inverted V ribs produce greater enhancement than all the other channels. Heat transfer enhancement (Nu ratio) over a smooth channel decreases with an increase in Reynolds number for all rib configurations at all locations.

4.6. Comparisons

Figure 8 compares the regionally averaged Nusselt number ratio distributions for the four configurations with and without bleed holes at $Re = 28\,500$. Results for the cases without bleed holes were presented by Ekkad and Han [12]. The values are almost identical in the first pass and second pass of the channel for channels with

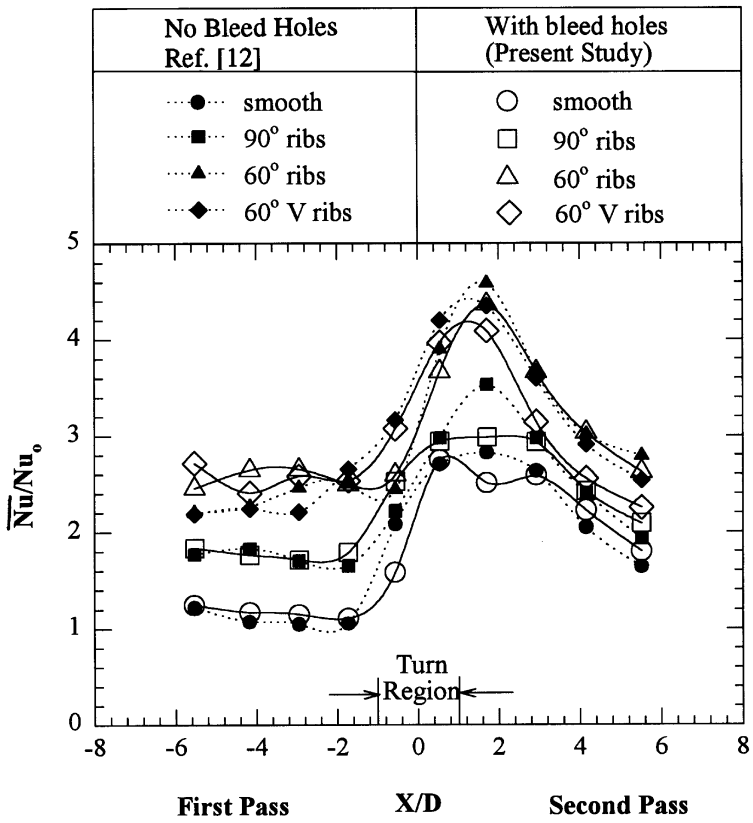

Fig. 8. Effect of bleed holes on regional-averaged Nusselt number ratio at $Re = 28\,500$.

and without bleed holes. It is important to note that the loss of 20–25% of the mainstream flow through the bleed holes (see Fig. 4) does not produce a reduction in regional averaged Nusselt number ratios compared to a channel without bleed holes. However, for the 60° parallel ribs and 60° V ribs, the Nusselt number ratios at $X/D > 3$ are lower for the channels with bleed holes compared with channels without bleed holes. The effect does not seem to be evident for the smooth and 90° ribbed channel. This indicates that 20–25% of the mainstream flow can be used to provide coolant for film cooling of the external blade surface from the first pass without reducing the level of the regional averaged Nusselt number ratio inside the channel. However, there are distinct variations in the detailed heat transfer distributions compared to channels without bleed holes (ref [12]). This indicates that the bleed holes tend to enhance heat transfer so that the level of Nusselt number ratios with bleed holes is about the same as that for a channel without bleed holes.

5. Conclusions

Local Nusselt number distributions are presented for turbulent flow in a two-pass square channel with bleed holes for smooth and ribbed walls using a transient liquid crystal technique. The detailed Nusselt number distributions help understand the heat transfer enhancement phenomena due to ribs and bleed holes. The conclusions based on the results presented are as follows:

1. A higher pressure drop across the channel produces lower bleed mass flow ratio. A smooth channel produces the lowest pressure drop but has the highest mass flow rate exiting out of the bleed holes.
2. Smooth channel Nusselt numbers are enhanced by the presence of bleed holes in the first pass due to tripping of flow at every hole location. However, the effect of bleed holes is reduced by the sharp 180° turn in the second pass due to decreased bleed.
3. For all ribbed channels, bleed holes enhance heat transfer around the hole edges in the first pass. However, the effect is reduced in the second pass due to the combined strong effects of the 180° turn and ribs similar to the smooth channel.
4. The 60° parallel ribs, 60° V, and 60° inverted V ribs produce similar high regional averaged heat transfer enhancement in the first pass. In the turn region, both 60° parallel ribs and 60° V ribs produce similar high heat transfer enhancement. The 60° inverted V ribs

produce the highest heat transfer enhancement in the second pass. A combination of 60° V rib in the first pass and a 60° inverted V rib in the second pass is expected to provide high heat transfer enhancement over the entire two-pass channel.

5. The loss of mainstream flow through the bleed holes (about 20–25%) does not cause any reduction in the average levels of Nusselt numbers in the two-pass channel. This indicates that coolant flow extracted through bleed holes for external blade surface film cooling produces very small changes in regional averaged heat transfer enhancement inside the turbulated cooling channel.

Acknowledgements

This paper was prepared with the support of the U.S. Department of Energy, Morgantown Energy Technology Center, Cooperative Agreement No. DE-FC21-92 MC 9061. The support of the technical team of Advanced Turbine Systems at Clemson University (Dr D. B. Fant and Dr L. P. Golan) is greatly appreciated. The project was also supported by the Texas Higher Education Coordinating Board—Advanced Technology Program under Grant 999903-165 (TEES 32190-71720ME).

References

[1] Han JC. Heat transfer and friction in channels with two opposite rib-roughened walls. ASME Journal of Heat Transfer 1984;106:774–81.
[2] Han JC. Heat transfer and friction characteristics in rectangular channels with rib turbulators. ASME Journal of Heat Transfer 1988;110:321–8.
[3] Han JC, Zhang YM, Lee CP. Augmented heat transfer in square channels with parallel, crossed, and V-shaped angled ribs. ASME Journal of Heat Transfer 1991;113:590–6.
[4] Han JC, Zhang YM. High performance heat transfer ducts with parallel, broken, and V-shaped ribs. International Journal of Heat and Mass Transfer 1992;35:513–23.
[5] Taslim ME, Li T, Kercher DM. Experimental heat transfer and friction in channels roughened with angled, V-shaped and discrete ribs on two opposite walls. ASME Journal of Turbomachinery 1996;118:20–28.
[6] Taslim ME, Wadsworth CM. An experimental investigation of the rib surface-averaged heat transfer coefficient in a rib-roughened square passage. ASME Journal of Turbomachinery 1997;119:381–9.
[7] Chandra PR, Niland ME, Han JC. Turbulent flow heat transfer and friction in a rectangular channel with varying number of ribbed walls. ASME Journal of Turbomachinery 1997;119:374–80.
[8] Chandra PR, Han JC, Lau SC. Effect of rib angle on local heat/mass transfer distribution in a two-pass rib-roughened channel. ASME Journal of Turbomachinery 1988;110:233–41.
[9] Chyu MK. Regional heat transfer in two-pass and three-pass passages with 180-deg sharp turns. ASME Journal of Heat Transfer 1991;113:63–70.
[10] Han JC, Zhang P. Effect of rib-angle orientation on local mass transfer distribution in a three-pass rib-roughened channel. ASME Journal of Turbomachinery 1991;113:123–30.
[11] Ekkad SV, Han JC. Local heat transfer distributions near a sharp 180° turn of a two-pass smooth square channel using a transient liquid crystal image technique. Journal of Flow Visualization and Image Processing 1995;2:285–97.
[12] Ekkad SV, Han JC. Detailed heat transfer distributions in two-pass square channels with rib turbulators. International Journal of Heat and Mass Transfer 1997;40:2525–37.
[13] Shen JR, Wang Z, Ireland PT, Jones TV, Byerley AR. Heat transfer enhancement within a turbine blade cooling passage using ribs and combinations of ribs with film cooling holes. ASME Journal of Turbomachinery 1996;118:428–34.
[14] Taslim ME, Li T, Spring SD. Experimental study of the effects of bleed holes on heat transfer and pressure drop in trapezoidal passages with tapered turbulators. ASME Journal of Turbomachinery 1995;117:281–9.
[15] Kline SJ, McClintock FA. Describing uncertainties in single-sample experiments. Mechanical Engineering 1953;75:3–8.